Reconstructing interfacial force distribution for identification of multi-debonding in steel-reinforced concrete structures using noncontact laser vibrometry

Hao Xu, Zhongqing Su, Li Cheng, Jean-Louis Guyader and Patrice Hamelin

Structural Health Monitoring 2013 12: 507 originally published online 11 September 2013
DOI: 10.1177/1475921713502837

Special Issue Article

SHM Structural Health Monitoring

Structural Health Monitoring
12(5-6) 507–521

DOI: 10.1177/1475921713502837
shm.sagepub.com
SAGE

Reconstructing interfacial force distribution for identification of multi-debonding in steel-reinforced concrete structures using noncontact laser vibrometry

Hao Xu[1,2], Zhongqing Su[1,2], Li Cheng[1,2], Jean-Louis Guyader[3] and Patrice Hamelin[4]

Abstract

Interfacial debonding in multilayered engineering structures can jeopardize the structural integrity without timely awareness. By reconstructing the distribution of interfacial forces and canvassing local perturbance to the structural dynamic equilibrium, an identification approach for interfacial debonding between different structural components was developed. A "debonding index," governed by the derivatives of reconstructed interfacial forces, was established, able to predict debonding in a quantitative manner including the coexistence of multi-debonding and their individual locations and sizes. The index offers the flexibility of detecting debonding between a beam-like component and its neighboring constituents of any type (beam, plate, shell, or even more complex components) with distinct material properties. To enhance the robustness of the approach under noisy measurement conditions, two denoising techniques (low-pass wavenumber filtering and adjustment of measurement density), together with a data fusion algorithm, were proposed. Using a noncontact laser vibrometry, the approach was validated experimentally by identifying multiple debonding zones in a steel-reinforced concrete slab dismantled from a bridge model. The approach has been demonstrated sensitive to debonding of small dimension owing to the use of high-order differential equation of motion. In addition, it does not require a global model of the entire system, prior information on structural boundaries, benchmark, baseline signals, and additional excitation sources as long as the structure undergoes steady vibration.

Keywords

Noncontact laser vibrometry, debonding, structural health monitoring, local dynamic equilibrium, denoising, data fusion, steel-reinforced concrete

Introduction

Concreted infrastructure experiences continuous accumulation of damage over the lifespan, as a result of manufacturing defect, improper use, service wearing, exposure to aggressive environment, insufficient maintenance, or even sabotage. They, consequently, deteriorate at an alarming rate, leading to catastrophic failure without timely inspection. Nowadays, more than 40% of the bridges in the United States are either structurally deficient or functionally obsolete, mainly because of accumulated damage and aging.[1] Allowing for exorbitant expense and difficulty in entirely rebuilding, there has been increasing preference to locally strengthen and retrofit the vulnerable areas of concreted infrastructure using materials with high specific strength and specific stiffness such as metal or polymer, configuring reinforced concrete structures to locally enhance the load resistance.[2]

Nevertheless, imperfect fabrication or excessive loads produced by foreign object impact can give rise

[1]The Hong Kong Polytechnic University Shenzhen Research Institute, Shenzhen 518057, PR China
[2]The Department of Mechanical Engineering, The Hong Kong Polytechnic University, Kowloon, Hong Kong SAR
[3]Laboratoire Vibrations Acoustique, Institut National des Sciences Appliquées (INSA) de Lyon, Lyon, France
[4]Laboratoire Genie Civil et Ingenierie Environnementale (LGCIE), University of Lyon 1, Lyon, France

Corresponding author:
Zhongqing Su, The Department of Mechanical Engineering, The Hong Kong Polytechnic University, Kowloon, Hong Kong SAR.
Email: MMSU@polyu.edu.hk

to interlaminar shear stresses that, if large enough, may cause separation of the metal or polymer layers from the concrete substrates, leaving a void at the interface, known as *debonding*. Debonding is probably the most common damage type in multilayered structures,[3–6] exerting detrimental effects on the stiffness and strength of the reinforced concretes for the discontinuity of load transfer.[7,8] That is because the overall capacity of a reinforced concrete is dependent substantially on the efficient load transfer through the adhesive at interfaces. Furthermore, an initial debonding can propagate rapidly under cyclic loads, from the tips of a debonded zone where particularly intense stress concentration exists, leading to severer failure of the whole structure.

Early detection of debonding warrants a safe and efficient service of the reinforced concrete structures, whereby the risk of structural integrity downgrade can be reduced considerably. To this end, appropriate nondestructive evaluation (NDE) must be ensured on a regular basis not only during installation but also throughout the intended service life of the reinforced concretes. Currently, the guidelines widely observed in the civil industry include material conformity check before installation, inspection of surface condition and adhesive curing during installation, and routine examination after installation,[9] using well-defined NDE techniques such as visual/tapping check, dummy samples testing, large-scale load testing, radioscopy, infrared thermography, ultrasonics, acoustic emission, and ground-penetrating radar.[10–15] However, these conventional NDE techniques suffer from bottlenecks such as limited access to geometrically complex structures, requirement of intensive labor, incurrence of high cost, and excessive sensitivity to ambient noise. They can generally be used for periodic inspection in an offline manner with demonstrated effectiveness in detecting debonding in small-scale infrastructural fragments only. These deficiencies have posed immediate urgency and aroused imperative needs for real-time and cost-effective surveillance so as to preclude possible debonding at early stage. In this aspect, a diversity of methods is readily available, dominated by global-vibration-based techniques[16–19] using, for example, eigen-frequencies,[20,21] mode shapes and modal curvature,[21–25] electromechanical impedance,[26,27] flexibility matrix,[28–30] and damping properties.[31] The rationale of these deployments resides on the fact that the occurrence of structural damage including debonding induces changes in physical properties of a structure (e.g. local stiffness, density, mass, thermal properties, and electromechanical impedance), and these changes are in turn manifested in the captured dynamic responses.

But implementation of these techniques for detection of debonding in reinforced concrete infrastructure can be somewhat hampered due to a number of obstacles, including their strong reliance on benchmark structures, baseline signals, global models, boundary conditions, and excitation sources. Under most circumstances, the dynamic responses are captured in a contact manner using embedded or attached transducers, which, however, may not be entertained in engineering practice. Most critically, such a global-vibration-based detection is insensitive to damage before it reaches a conspicuous extent because damage is a local event which would not alter global responses prominently.[32]

Motivated by the above recognition and residing on the authors' previous work pertaining to reconstructing distribution of excitation force[33,34] and damage modeling for beam-like[35] and plate-like[36] structures, a novel identification approach for predicting debonding in steel-reinforced concrete structures was developed, by canvassing local perturbance to the structural dynamic equilibrium. A "debonding index" (*DI*) governed by the derivatives of reconstructed interfacial forces between constituents was established, able to indicate the individual locations and sizes of multiple debonding zones. Different denoising treatments including low-pass wavenumber filtering (LWF), adjustment of measurement density (AMD), and a data fusion algorithm were proposed to enhance the practicability of the approach. Experimental validation was carried out by identifying multi-debonding zones in a steel-reinforced concrete structure dismantled from a bridge model.

Principle of methodology

Given a structural component, its steady vibration can be described in general by

$$[\mathbf{L}] \cdot [\mathbf{u}] = [\mathbf{F}] \cdot \delta(M - M_e) \tag{1}$$

where $[\mathbf{L}]$ is a matrix differential operator, $[\mathbf{u}]$ the structural displacement, $[\mathbf{F}]$ the external excitation force applied on the surface of the component at location M_e, and δ a Dirac function which vanishes at M when $M \neq M_e$. For a free surface in the absence of any external excitation, the left-hand-side term of equation (1) equals to zero provided the structure is free of damage. With measured $[\mathbf{u}]$, any drastic deviation from zero in the left-hand-side term at a particular spatial position M implies, in principle, local breakage of the structural equilibrium, that is, occurrence of damage therein. Without loss of the generality, now consider a homogeneous isotropic Euler–Bernoulli beam-like component. Equation (1) can be specified for the beam component, in a harmonic regime, as

$$EI\frac{\mathrm{d}^4 w(x)}{\mathrm{d}x^4} - \rho S\omega^2 w(x) = N(x) + \frac{\mathrm{d}\left(\frac{h}{2}\cdot T(x)\right)}{\mathrm{d}x} \tag{2}$$

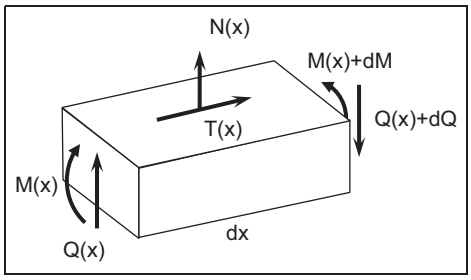

Figure 1. Schematic of internal forces and moments for a beam-like component.

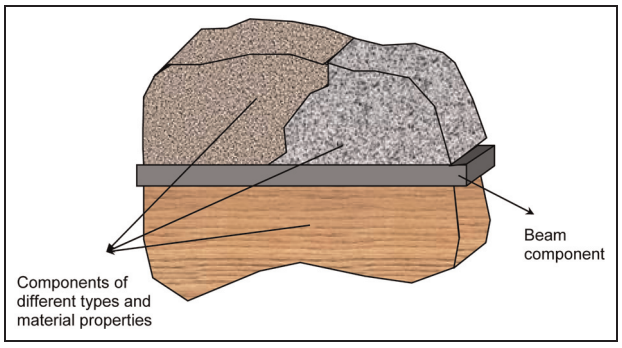

Figure 2. Schematic of a multilayered system comprising a beam-like component and other constituents of different types.

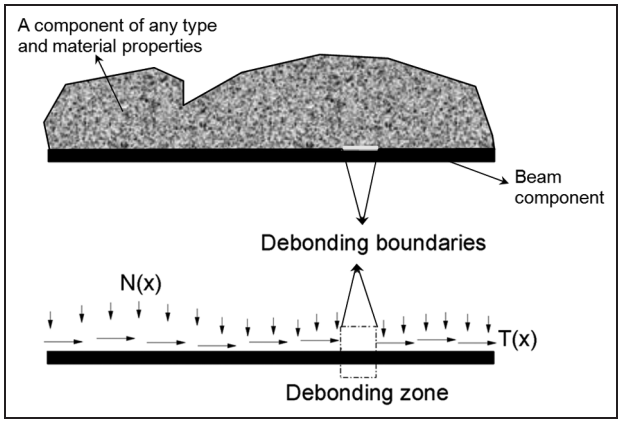

Figure 3. Schematic of internal force distributions at the interface between a beam-like component and its neighboring component of any type and material properties.

where $w(x)$ is the transverse displacement of the component at x; E, ρ, I, S, and h are Young's modulus, density, moment of inertia, area of cross-section, and thickness of the beam component in its intact status, respectively; ω is the angular frequency of the vibration; $N(x)$ and $T(x)$ are the density of external force applied on the component surface at x in normal and tangential directions, respectively, as shown schematically in Figure 1. Equation (2) locally applies to every single point of the beam component, therefore serving as a local equilibrium indicator linking the inertia forces of the beam component to external forces. Even in the absence of any external force, equation (2) is still tenable, locally describing the forced vibration of a beam component driven by the internal forces exerted by its adjacent elements.

The above discussion can be extended to a multilayered system with at least one layer which can be characterized as a beam component, whereas the remaining layers can be of different components with distinct material properties, as illustrated schematically in Figure 2. The beam component layer interacts with its neighboring layers through the internal forces ($N(x)$ and $T(x)$ in equation (2)) at the sharing interfaces. Note that these interfacial forces are "external" forces to the beam component under investigation from its adjacent layers, and thus called *pseudo-external forces* in what follows.

The presence of a debonding at the interface as shown in Figure 3 significantly decreases both $N(x)$ and $T(x)$ within the debonding zone because of the discontinuity of stress transfer therein, and this leads to singularity in the distribution of $N(x)$ and $T(x)$. The debonding also incurs fluctuation in the left-hand-side term of equation (2) at boundaries of the debonding zone, reflected by the derivative of the interfacial force $((\mathrm{d}T(x))/\mathrm{d}x)$. Such an attribute of equation (2) can be conducive to estimating the location and subsequently the size of a debonding zone. Based on this, a *DI* is defined as

$$DI = EI\frac{\mathrm{d}^4 w(x)}{\mathrm{d}x^4} - \rho S\omega^2 w(x) \tag{3}$$

namely, the left-hand-side term of equation (2). The flexural displacement ($w(x)$) is the only parameter needed to construct the *DI*.

Note that the material properties (E and ρ) and geometric parameters (I and S) as well as $w(x)$ are those associated with the beam component only, regardless of the complexity of the rest of the multilayered system with which the beam is associated. This trait endows the *DI* with flexibility of predicting debonding at the interface between a beam component and neighboring constituents of any type (beam, plate, shell, or even more complex components) with distinct material properties. The proposed *DI* claims somewhat convenience in the selection of excitation frequency. Provided the excitation is not harmonic and spans over a certain frequency bandwidth instead, a frequency component in the frequency domain after Fourier transform can be extracted, at which the *DI* is constructed.

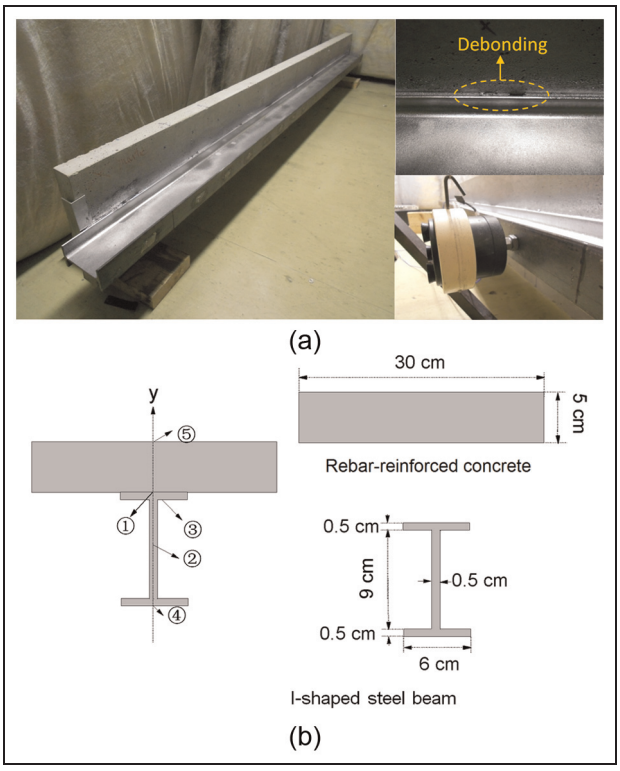

Figure 4. (a) A concrete slab reinforced with an I-shaped steel beam and (b) cross-section of the reinforced concrete slab.

Table 1. The location and size of debonding zones in the steel-reinforced concrete slab.

Number of debonding zones	Location (left boundary, right boundary)[a]	Size[b] (%)
D_1	(400, 430)	1.3
D_2	(650, 690)	1.7
D_3	(890, 940)	2.1
D_4	(1160, 1230)	3.0
D_5	(1450, 1500)	2.1
D_6	(1705, 1745)	1.7
D_7	(1950, 1980)	1.3

[a]In the coordinate system shown in Figure 5.
[b]The ratio of the length of the debonding zone to the total length of the beam span.

The independence of the approach on selection of excitation frequency endows $w(x)$ with certain flexibility—$w(x)$ can be either the mode shape of the structure at a specific natural frequency or the flexural displacement under an arbitrarily selected frequency. Optimal selection of ω is to be discussed in subsequent sections. Although the system damping is apprehended in modulus E, estimate of the damping is tedious in practice and its effects can become pronounced only in the vicinity of the resonance region. Therefore, it is preferable to construct the DI at an off-resonance regime of the multilayered system, so as to minimize the effect of system damping.

During practical implementation, $w(x)$ can be obtained discretely at a dense set of spatial points closely spaced along the beam span (corresponding to measurement points in experiment), to approximate $(\mathrm{d}^4w(x))/\mathrm{d}x^4$ in equation (3) for constructing the DI using the finite difference. Thus, the DI at measurement point i (denoted by DI_i) reads

$$DI_i = \frac{EI}{d_m^4}\left(w_{i+2} - 4w_{i+1} + 6w_i - 4w_{i-1} + w_{i-2}\right) - \rho S\omega^2 w_i \tag{4}$$

if four neighboring measurement points from point $i-2$ to $i+2$ are involved. In equation (4), w_i is the measured transverse displacement at point i, and similar to other displacement variables; d_m stands for the interval between two adjacent measurement points.

Characterization of multi-debonding in steel-reinforced concrete structure

The above DI was validated by quantitatively evaluating multiple debonding zones in a concrete slab reinforced by a steel beam as shown in Figure 4(a), which was dismantled from a bridge model.

Problem description

The concrete slab, 2350 mm long and simply supported at its two ends, was reinforced externally with an I-shaped steel beam and internally with rebars (rebar reinforcement ratio: 2.5% by volume). The slab was preinspected to warrant free of observable spalling, crack, and other types of gross defects. A total of seven width-through debonding zones (D_1–D_7) were scattered at the interface between the concrete slab and the steel beam, with individual locations and sizes tabulated in Table 1. As explained previously, as long as a beam component is concerned, the complexity of the residual of the multilayered system (e.g. inhomogeneous and anisotropic nature of the concrete, or rebars inside) would not dilute the validity of the DI.

Feasibility study using numerical simulation

Characteristics of the DI and its accuracy for predicting debonding were first examined using finite element (FE) simulation. The system was modeled in its full scale using three-dimensional brick elements, as displayed in Figure 5. To canvass the interfacial forces, the interface was particularly refined, where each element

Table 2. Material properties of the concrete and steel used in numerical simulation.

	Concrete	Steel
Young's modulus, E (GPa)	24	200
Density, ρ (kg/m^3)	2700	7800
Poisson's ratio, ν	0.2	0.27
Damping ratio, ξ	0.01	0.002

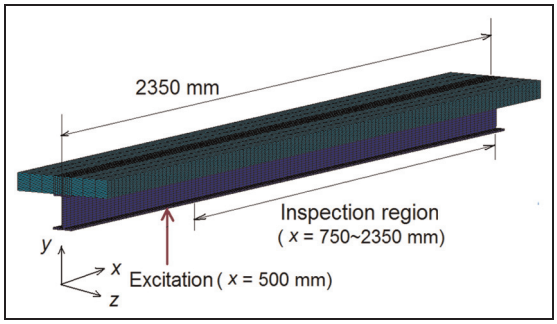

Figure 5. Finite element model of the reinforced concrete slab shown in Figure 4(a) bearing a simulated debonding region.

measured $20 \times 2.5 \times 2.5\,\text{mm}^3$. As explained previously, any component adjacent to the beam component is not of interest with no contribution to the construction of the *DI*. Thus, modeling of the concrete slab was simplified by assuming an isotropic and homogeneous nature with the material properties given in Table 2. A point force, perpendicular to the steel beam surface and 500 mm from the left beam end, excited the beam at an arbitrarily selected frequency of 600 Hz. It is relevant to note that the excitation can also be a wideband signal, ambient vibration, or even white noise, as long as the structure undergoes steady vibration. A frequency component in the frequency domain after Fourier transform can be selected, and then advanced measurement means (e.g. laser vibrometer) can be employed to capture signal components associated with the selected frequency. In this connection, additional excitations are not of necessity, and in contrast the vibration can be driven by "natural" sources such as the traffic loads applied to a bridge.

A width-through debonding zone was assumed at the interface, 300 mm long and 1600 mm from its center to the left beam end. Such a severe debonding scenario (~12.8% of total interfacial area) was aimed at comprehending the characteristics of the *DI*. To eliminate possible singularity near the excitation source, an inspection region (750–2350 mm) was defined as indicated in Figure 5, and the *DI* was constructed in the inspection region only. The simulation was carried out using the commercial FE code ANSYS®. To the beam, the normal and tangential interfacial forces, denoted by f_N and f_T, respectively, are *pseudo-external forces* exerted by the concrete slab, which were obtained by calculating the nodal forces at the middle line of the interface (indicated by "①" in Figure 4(b)) along the beam span, and the results are shown in Figure 6. Note that f_N and f_T were extracted from the nodes at "①" which can be deemed, respectively, as the means of $N(x)$ and $T(x)$ across the beam width. Therefore, $N(x) + (h/2) \cdot (\mathrm{d}T(x)/\mathrm{d}x)$ in equation (2) can be

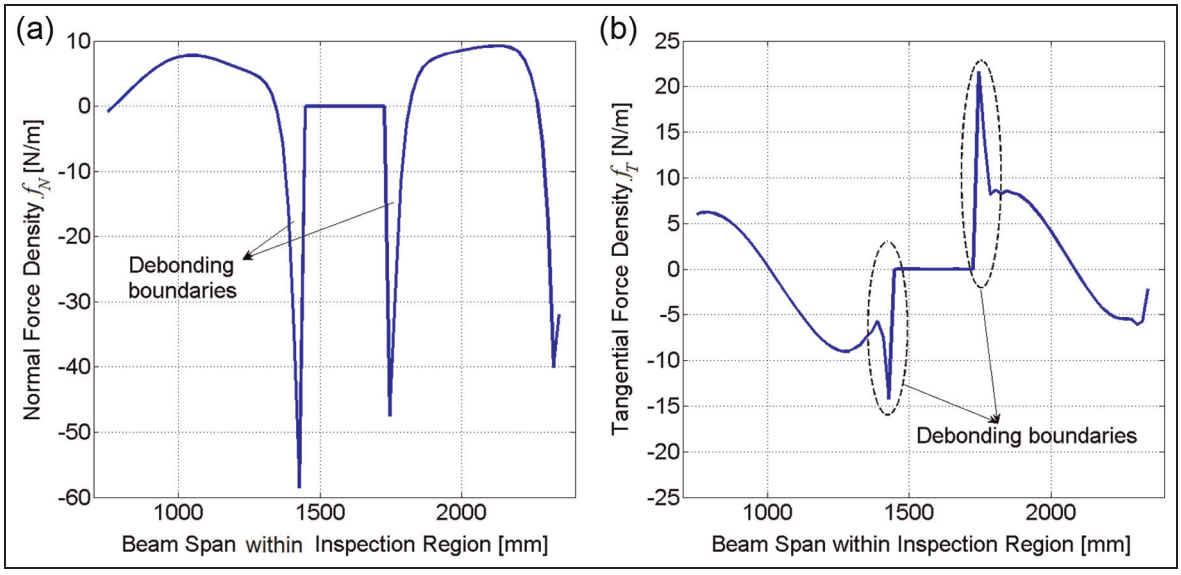

Figure 6. Distributions of (a) the normal nodal force density, f_N, and (b) the tangential nodal force density, f_T, within the inspection region.

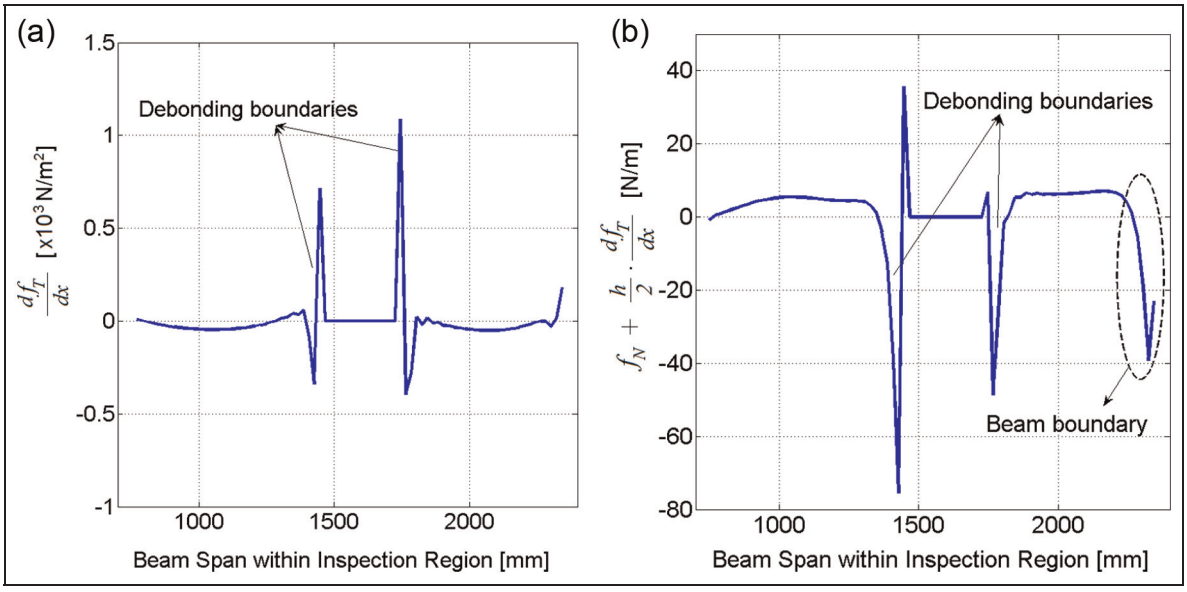

Figure 7. Distributions of (a) the derivative of the tangential nodal force density, df_T/dx, and (b) the right-hand-side term of equation (2).

approximated with $f_N + (h/2) \cdot (df_T/dx)$. In Figure 6, discontinuities in f_N and f_T can clearly be observed at the two ends of the debonding zone; both retreat to none within the debonding area because of the interruption in transfer of interfacial forces therein. This interruption resulted in drastic oscillations of the derivatives of f_N and f_T at the debonding boundaries, as shown in Figure 7(a) for df_T/dx as an example. Figure 7(b) further displays $f_N + (h/2) \cdot (df_T/dx)$, revealing (a) prominent elevation of $f_N + (h/2) \cdot (df_T/dx)$ takes place at the boundaries of the debonding zone only; while (b) $f_N + (h/2) \cdot (df_T/dx)$ features a smooth variation with regard to zero over the majority of the inspection region; and (c) it turns to zero within the debonding zone. Note that the singularity near the beam ends can also be observed which can be attributed to the insufficient measurement points therein for finite difference calculation (known as the *Gibbs phenomenon*[34]).

For discussion, w_i was extracted from the nodes at "②" (see Figure 4(b)) by calculating the nodal displacement and is displayed in Figure 8(a), with the correspondingly constructed *DI* in Figure 8(b) using equation (4). It is noteworthy that the distribution trait of the *DI* as observed in Figure 8(b) possesses high resemblance with the curve of $f_N + (h/2) \cdot (df_T/dx)$ in Figure 7(b), although in different scales because the nodal forces in Figure 7(b) are the means of $N(x)$ and $T(x)$ across the beam width at "①" whereas w_i is the flexural displacement at the mass center of the I-shaped beam at "②" This consistency between Figure 7(b) (i.e. the right-hand-side term of equation (2)) and Figure 8(b) (namely, the *DI*, also the left-hand-side term of equation (2)) has corroborated the theoretical basis described by equation (2) from which the *DI* was developed.

For further comparison, w_i was also extracted from the nodes at "①" "③" "④" and "⑤" respectively, and the correspondingly constructed *DIs* are shown in Figure 9(a) to (d). It is important to note that the *DI* with w_i at or close to the interface (① in Figure 9(a) and ③ in Figure 9(b)) manifests more drastic oscillation at the debonding boundaries due to more significant stress singularities at these two positions. In addition, allowing for the difficulty in acquiring the vibration deflections right at the interface in practical measurement, w_i at ③ would be most conveniently captured for constructing the *DI*, which was the case in the following experiments. Note that calculation of *DI* involves neighboring measurement points beyond the actual debonding region, leading to overestimated debonding size.

The above results of FE simulation have demonstrated the feasibility of using the proposed *DI* for evaluating interfacial debonding in a quantitative manner regardless of the complexity of the coupled concrete and also unraveled the attributes of the *DI* distribution in the intact and debonding zones, as well as at the debonding boundaries.

Characterization of debonding using experiment

A scanning Doppler laser vibrometer (Polytec PSV-400B) was employed to measure w_i of the steel beam at ③ in a contactless manner. Considering its long

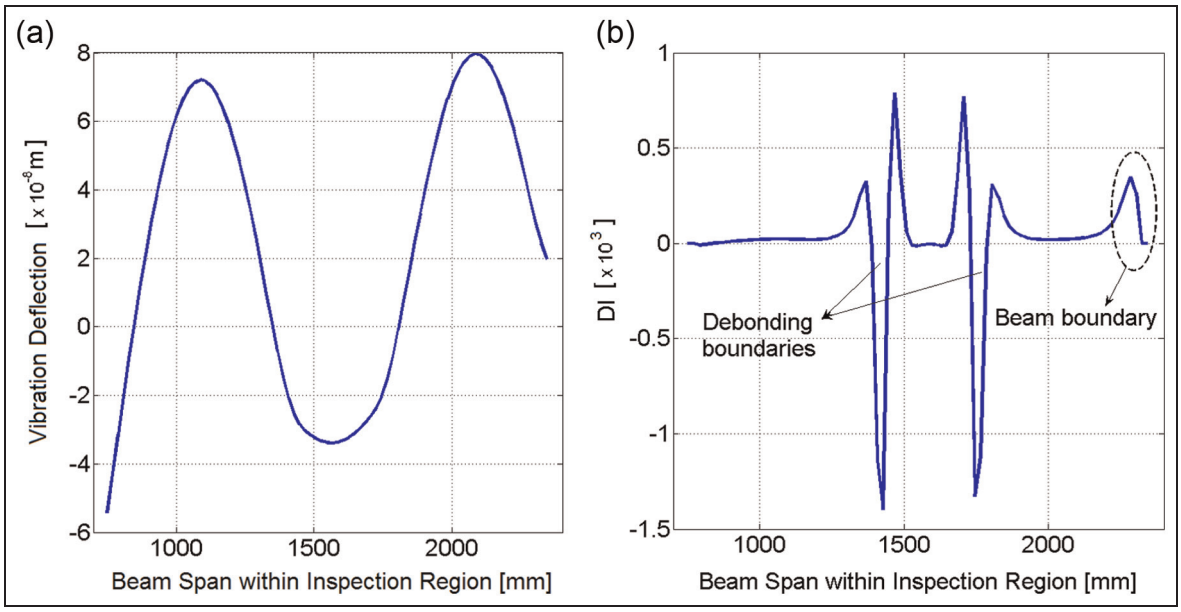

Figure 8. (a) The vibration deflection captured from the nodes at "②" and (b) the correspondingly constructed *DI* within the inspection region.
DI: debonding index.

span, the reinforced slab was divided into the left (320–1325 mm) and right (1145–2140 mm) inspection regions with a slight overlap, as in Figure 10. For the right inspection region, a point force excitation source was 480 mm away from the left beam end (E_1 in Figure 10), while 1845 mm for the left region (E_2). The excitation force was generated by an electromechanical shaker, as shown in Figure 4(a). w_i under four arbitrarily selected excitation frequencies (800, 1200, 2000, and 3000 Hz) was captured using the laser vibrometer, and those for the right inspection region are exhibited in Figure 11 for illustration. Thirty-time averaging was applied to raw data to screen random measurement noise. Note that these frequencies were selected arbitrarily to testify the independence of the approach of vibration frequency. At higher frequencies w_i presents more nonperiodical property (mainly contributed by the lower frequency components of the steel-concrete-coupled system under higher excitation frequencies), as a combined result of the coupling effect of the concrete on the vibration of the steel beam at higher frequencies. It is noteworthy that such a phenomenon is not evidenced in the signals from simulation because the above simplified FE model does not account for the coupling effect between the steel and the concrete slab.

Figure 12(a) to (d) shows the *DI* (absolute values) accordingly constructed using w_i in Figure 11(a) to (d) upon signal averaging, respectively. However, an attempt to observe oscillation of the *DI* at the debonding boundary turned to be impossible as a consequence of the noise contamination. It is the connatural nature of the *DI* which involves higher-order derivatives of the vibration signal (i.e. $(d^4w(x))/dx^4$) leading to such high vulnerability of the *DI* to noise. The noise components in w_i can become dominant upon the fourth-order differentiation, dimming debonding-incurred abnormality. It is thus of vital necessity to apply proper denoise treatments. Compared with noise influence, the nonperiodical vibration of the steel-concrete-coupled system, exhibited under higher excitation frequencies as shown in Figure 11(c) and (d), does not remarkably influence the constructed *DIs*, as observed in Figure 12. It is relevant to note that the contact effect between the concrete and the steel beam due to the debonding was not considered in simulation, accounting for the discrepancy between experimental and simulation results.

Denoising techniques

LWF. Based on the fast Fourier transform (FFT) of the *DI* from the spatial to the wavenumber domain, the LWF can be explained as a low-pass filter to eliminate the signal components in higher wavenumber domain that are vulnerable to measurement noise, while remain those in lower wavenumber domain which preserve signal features associated with the damage. In the LWF, a filter function is defined, in the wavenumber domain, as

$$\begin{aligned} \tilde{h}(k) &= 1, \quad (k \in [-k_c, +k_c]) \\ \tilde{h}(k) &= 0, \quad (k \in [-\infty, -k_c] \cup [+k_c, +\infty]) \end{aligned} \tag{5}$$

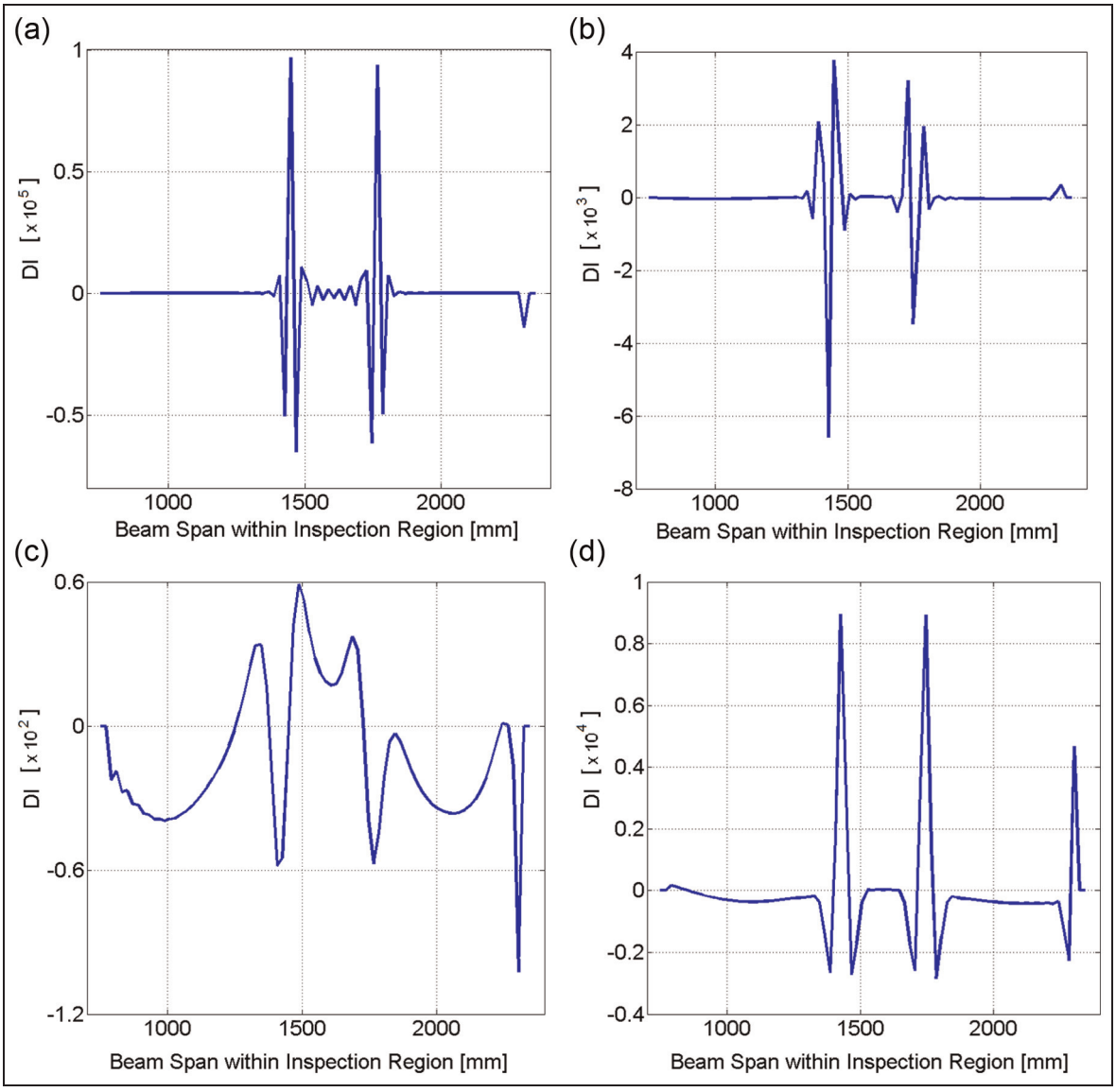

Figure 9. Constructed *DI* using the vibration deflections captured at (a) "①" (b) "③" (c) "④" and (d) "⑤".
DI: debonding index.

where k represents the wavenumber, and k_c with a unit of rad/m is the cut-off wavenumber serving as a threshold. To eliminate the Gibbs phenomenon at the beam ends, a one-dimensional rectangular window function was applied to the *DI* in the spatial domain prior to the above wavenumber filtering, which reads

$$\begin{aligned}
&\Psi(x) = 0.5 \times \left(1 - \cos\frac{\pi x}{\alpha}\right), \quad (x < \alpha) \\
&\Psi(x) = 1, \quad (\alpha \leqslant x \leqslant L_{\text{Inspection}} - \alpha) \\
&\Psi(x) = 0.5 \times \left(1 - \cos\frac{\pi \cdot (x - L_{\text{Inspection}} + 2\alpha)}{\alpha}\right), \\
&\qquad (x > L_{\text{Inspection}} - \alpha)
\end{aligned} \tag{6}$$

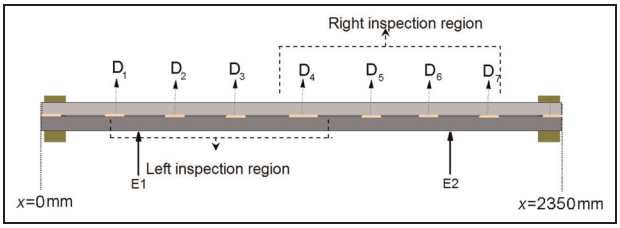

Figure 10. Schematic of experimental setup, showing the left (with excitation at E_2) and right inspection regions (with excitation at E_1).

where $\alpha = 2\pi/k_c$, and $L_{\text{Inspection}}$ is the length of the inspection region. Upon application of the rectangular

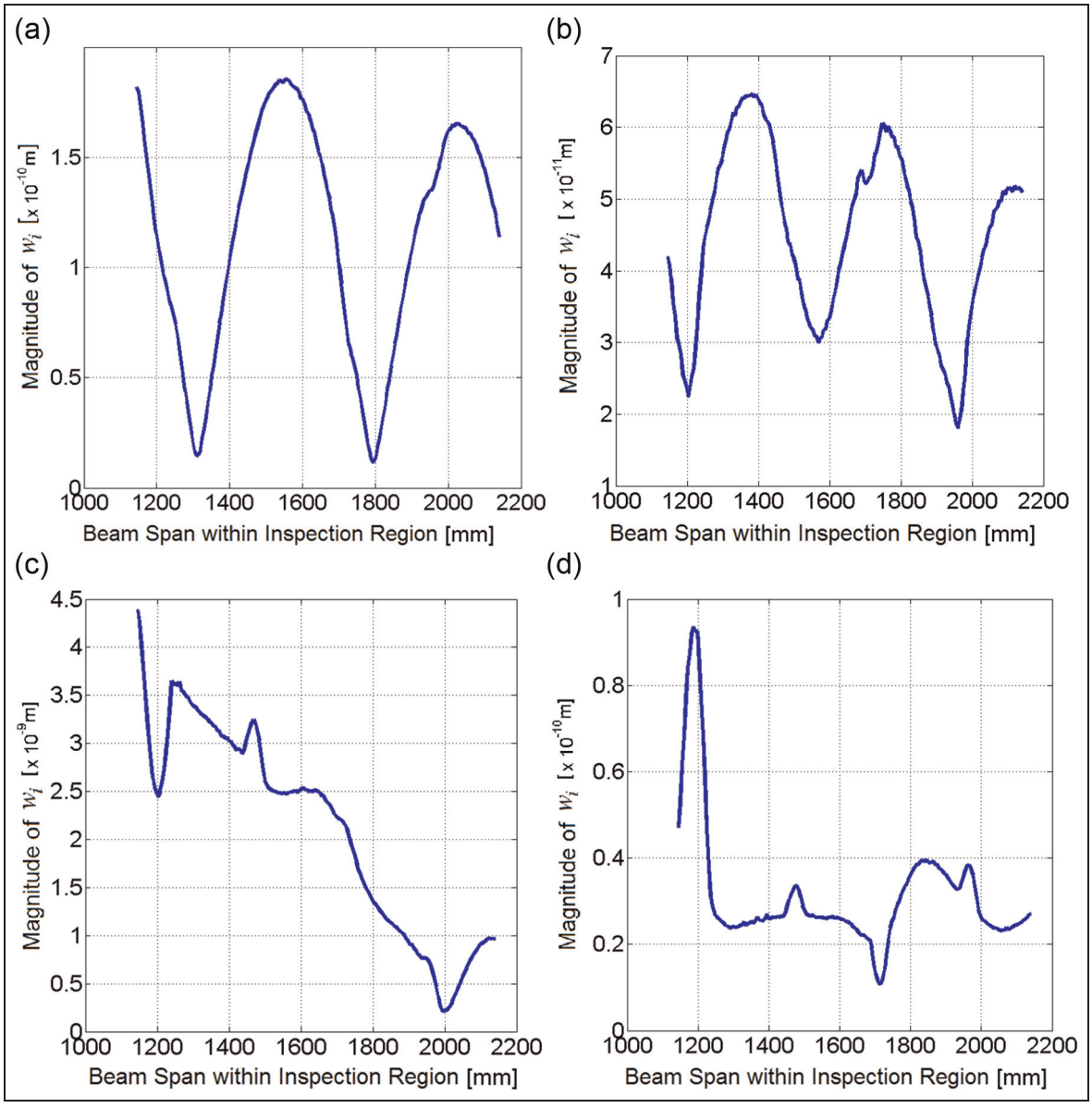

Figure 11. Magnitudes of w_i under (a) 800, (b) 1200, (c) 2000, and (d) 3000 Hz (results are shown for the right inspection region only).

window and then the LWF to the *DI* (absolute values) constructed using w_i captured at ③ (Figure 11), Figure 13 shows the reconstructed *DI* through an inverse FFT (k_c was set as 150 rad/m). Compared with those in Figure 12 without the LWF processing, the results in Figure 13 show much improved detection accuracy, particularly under the excitation frequencies of 2000 and 3000 Hz, in which the locations and sizes of most debonding zones are revealed. The discrepancy among the results in Figure 13(a) to (d) can be attributed to the fact that the distribution of the *DI* is closely related to the traits of interfacial forces along the beam span which are governed by a variety of factors including, for example, the position and frequency of the excitation source. A selection of higher excitation frequency is observed to generally offer improved detection resolution, as shown in Figure 13(d). Note that an inappropriate selection of the filtering window (i.e. inappropriate k_c in equation (5)) can result in signal feature lose, and a detailed description on selection criteria can be referred to elsewhere.[35] It has also been noted that the results in Figure 13 are not accurate to reveal all debonding regions, entailing further denoising treatment as described in the following sections.

AMD. Alternatively, the influence of measurement noise on the *DI* can be minimized by optimally maneuvering

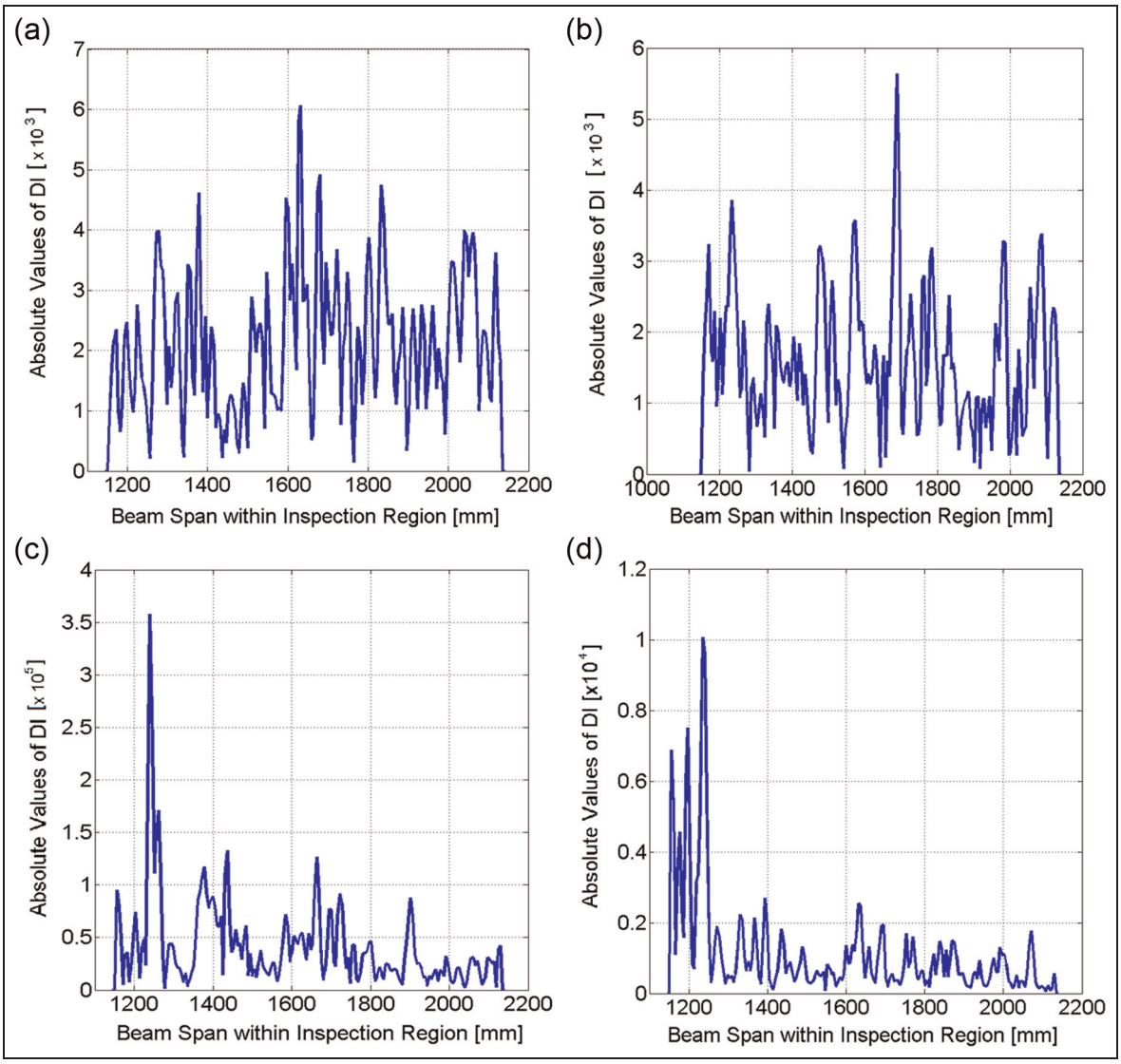

Figure 12. Constructed *DI* (absolute values) using vibration deflections under (a) 800, (b) 1200, (c) 2000 and (d) 3000 Hz (without any denoising treatment) (results are shown for the right inspection region only).
DI: debonding index.

the ratio of the distance between two adjacent measurement points (d_m) to the wavelength of vibration (λ), a measure called AMD in this study. It is well understandable that the accuracy of finite difference for calculating DI_i using equation (4) decreases as an increase in d_m (less measurement points); on the contrary, the noise influence on DI_i reduces as d_m increases because the noise in w_i can be strengthened considerably after the fourth-order differentiation. Thus, noise influence can be minimized by merely adjusting the density of measurement points (namely, optimizing d_m) and striking a balance between the accuracy of finite difference and the noisy immunity of the *DI*.

It has been demonstrated by the authors[36] that with a level of noise level less than 5% of the magnitude of w_i (the common cases using a scanning Doppler laser vibrometer), around 10 measurement points per wavelength (i.e. $d_m/\lambda = 0.1$) can be deemed as the most optimal selection to reach the above balance. Figure 14 shows the constructed *DI* using w_i in Figure 11, by reducing the number of measurement points evenly distributed within the inspection region from 189 ($d_m = 5.3$ mm, those cases in Figure 12) to 48 ($d_m = 21.2$ mm, tallying with the criterion of $d_m/\lambda = 0.1$), to observe prominent noise suppression and therefore enhanced detectability, compared with those results in Figure 12 without any denoising treatment. The AMD-processed results allow explicit indication of locations and sizes of individual debonding zones, although the detection resolution varies subject to the excitation

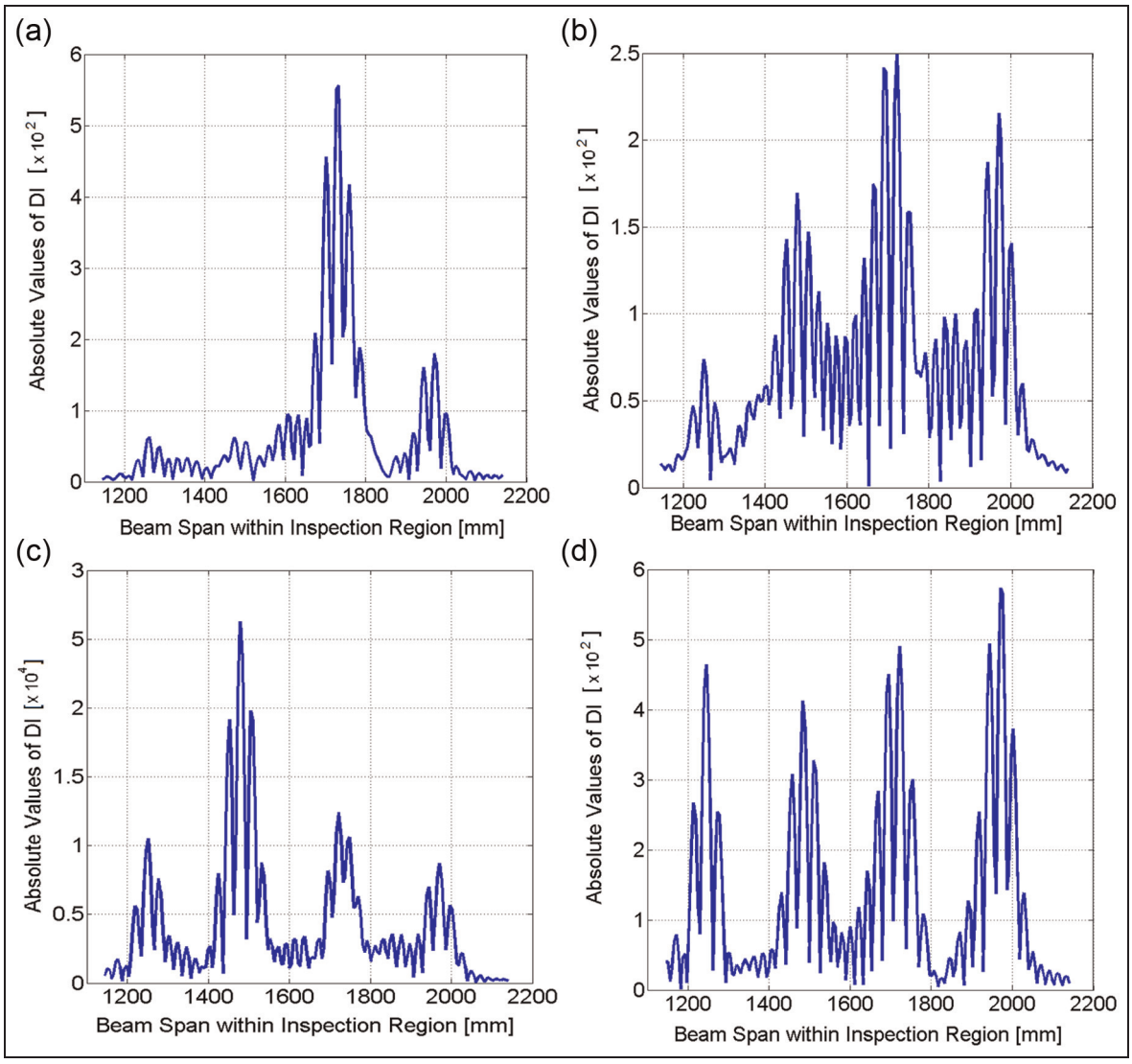

Figure 13. Reconstructed *DI* (absolute values) upon application of LWF using vibration deflections under (a) 800, (b) 1200, (c) 2000, and (d) 3000 Hz (results are shown for the right inspection region only).
DI: debonding index.

frequency (a higher excitation frequency ends up with a finer detection resolution (from Figure 14(a) to (d)).

Data fusion. Implementation of the proposed *DI* is not limited by measurement configurations per se. Instead it can be manipulated under a variety of experimental deployments, for example, under different excitation frequencies and different measurement densities with or without use of LWF or AMD. Such flexibility and adaptability of the *DI* enable a series of detection results and formation of a data pool. An extreme scenario can be the case that the structure is excited in a broad frequency band in a single test and construction of *DI* is subsequently conducted using the vibration signals extracted under individual frequencies. To exploit such a merit, a data fusion algorithm was additionally developed to enhance the toleration of the *DI* to measurement noise. Assuming DI_i can be ascertained under K different measurement configurations (denoted by $DI_{i-1}, DI_{i-2}, DI_{i-L}, \ldots, DI_{i-K}$ $(L = 1, 2, \ldots, K)$, the algorithm is expressed as[37,38]

$$DI_{i-\text{ultimate}} = \left[\frac{1}{K}\sum_{L=1}^{K} DI_{i-L}\right] \cap \left[\sqrt[K]{DI_{i-1} \cdot DI_{i-2} \cdots DI_{i-L} \cdots DI_{i-K}}\right] \quad (7)$$

where $DI_{i-\text{ultimate}}$ is the ultimate DI_i. The first part ("Σ" in the equation) of the algorithm is an arithmetic

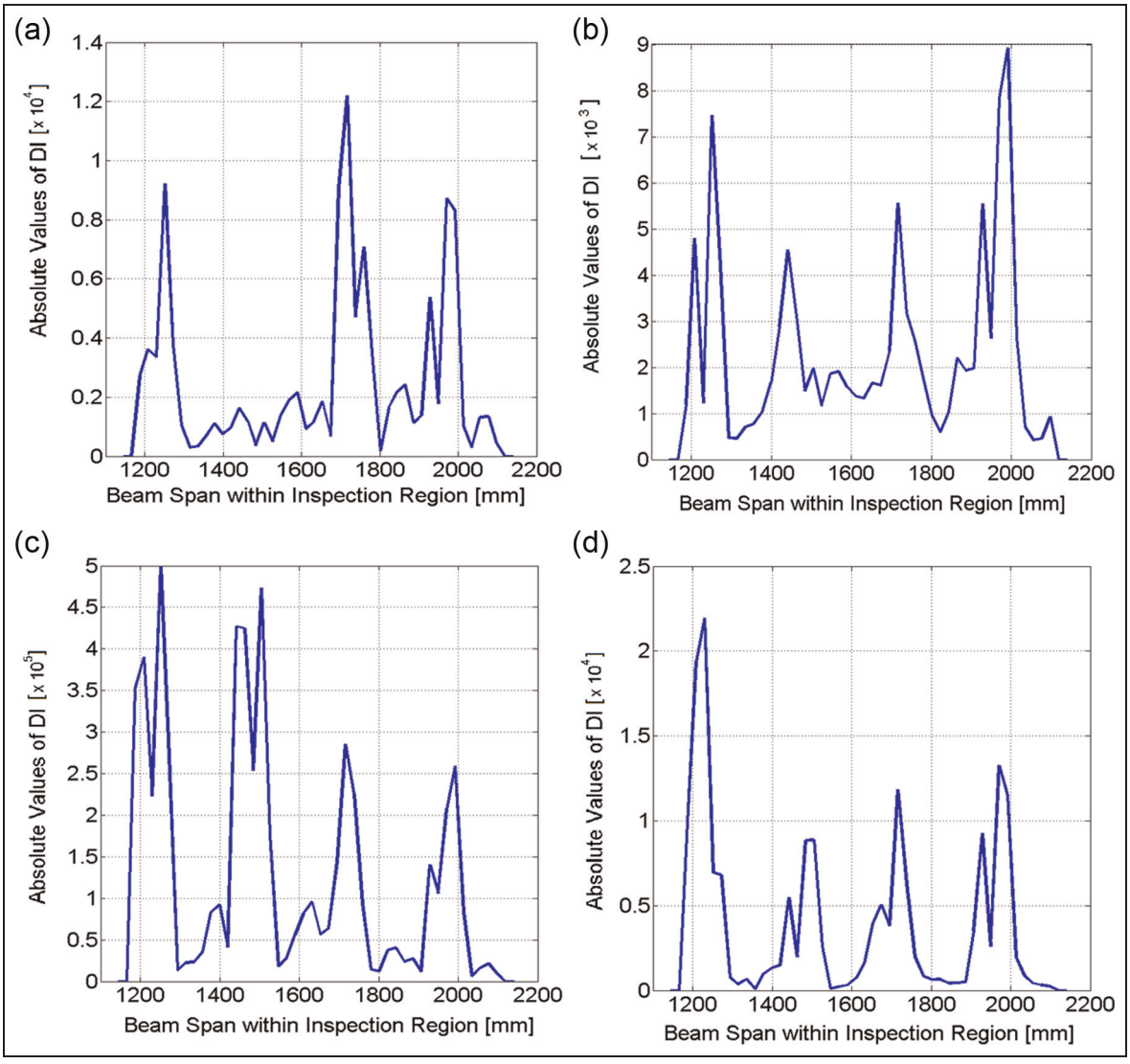

Figure 14. Constructed *DI* (absolute values) upon application of AMD using vibration deflections under (a) 800, (b) 1200, (c) 2000, and (d) 3000 Hz (reducing the number of measurement points from 189 in Figure 12 to 48) (results are shown for the right inspection region only).
DI: debonding index.

fusion, which equally takes into account all prior perceptions pertaining to the damage established under different measurement configurations and well decentralizes individual contributions to $DI_{i-\text{ultimate}}$. However, ambient noise and measurement uncertainties are also included in the arithmetic fusion, potentially to "pessimistically exaggerate" the possibility of debonding presence and lead to a false alarm. To circumvent this deficiency, the results from arithmetic fusion are equipoised with a geometric mean ("$\sqrt[K]{\ }$" in equation (7)) and further a conjunctive fusion ($\cap$), to reach a compromise between the arithmetic and geometric fusion, by equally considering the perceptions from all source information whereas appropriately decentralizing their contributions. This fusion algorithm enables a prominence of the salient features in common (i.e. those pertaining to damage) and meanwhile suppression of less salient features in individuals (e.g. measurement noise).

Applied with the above data fusion algorithm, $DI_{i-\text{ultimate}}$ in the left and right inspection regions is shown in Figure 15(a) and (b), respectively, using eight groups of results treated by LWF (Figure 13(a) to (d) for the right inspection region; similarly for the left region) and by AMD (Figure 14(a) to (d) for the right inspection region; similarly for the left region). Both figures clearly and accurately show the debonding cases in the concrete slab with respective location and

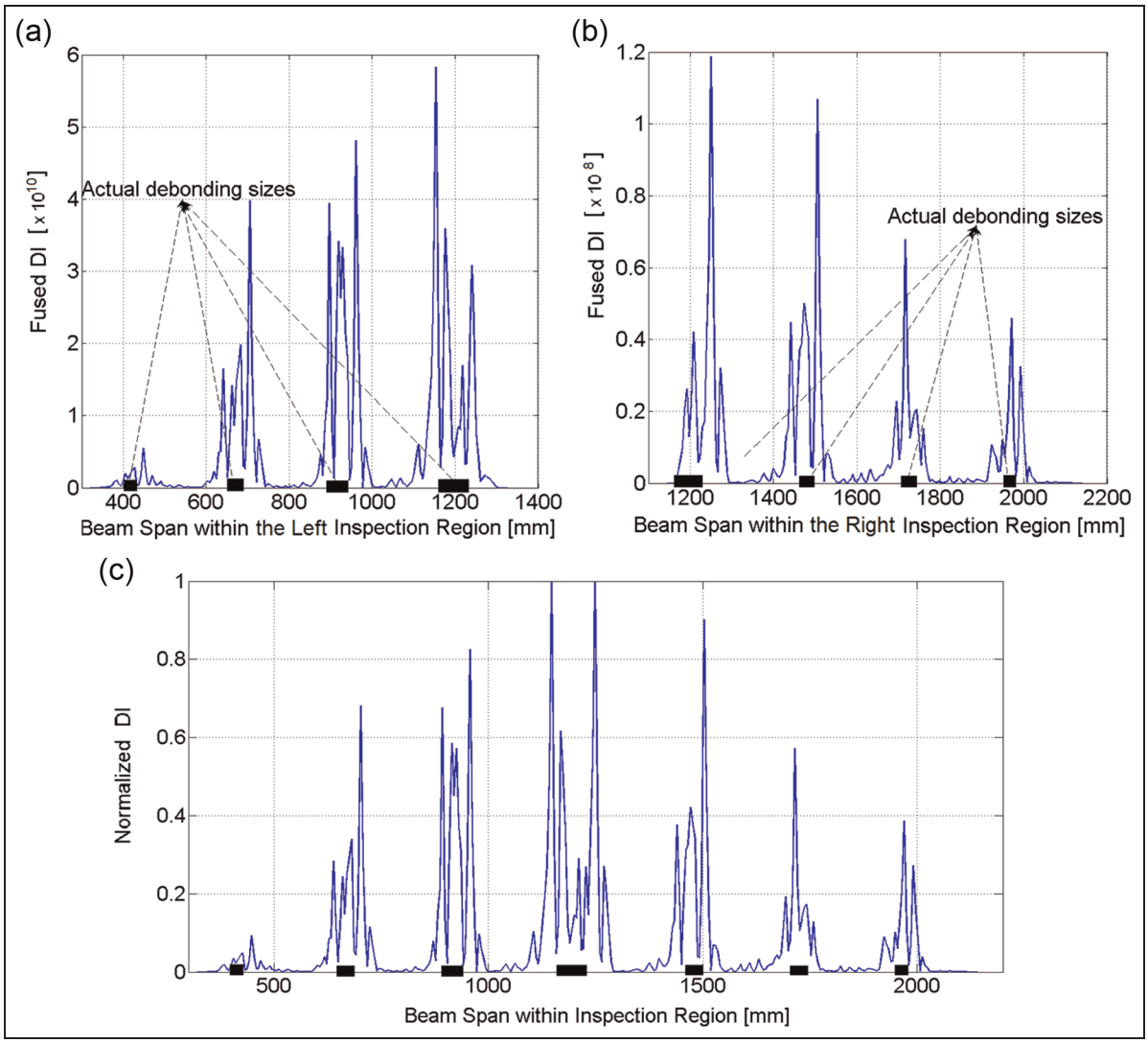

Figure 15. Fused *DI* (absolute values) within the (a) left and (b) right inspection regions and (c) the normalized ultimate *DI* within the inspection region of the whole slab.
DI: debonding index.

approximate size, although the predicted debonding sizes are greater than actual sizes due to the noise interference. Compared with the results shown in Figures 13 and 14, significantly "narrowed" prediction on the debonding size can be observed in the fused results, with less false fluctuation. It is also interesting to note that either in the left or in the right inspection region, the absolute values of the *DI* show a decrease tendency with an increase in the distance from the excitation source because, at a given debonding size, both the internal bending moments and the interfacial forces decrease. Finally, by normalizing the *DI* in Figure 15(a) and (b) and combining both, the ultimate detection results for the entire inspection region are given in Figure 15(c), highlighting all debonding zones in the concrete slab. Note that detailed discussion on LWF, AMD, and data fusion can be referred to elsewhere.[35]

Conclusion

A detection approach for interfacial debonding in multilayered systems was developed by reconstructing the interfacial forces and canvassing local perturbance to the structural dynamic equilibrium. The compelling features of this method lie in its independence of a global model for the entire system, no need of prior information on structural boundaries, benchmark, baseline signals, and additional excitation sources. A DI was proposed with demonstrated effectiveness in characterizing the debonding in a quantitative manner including

the coexistence of multi-debonding and their individual locations and sizes. It offers the flexibility of predicting debonding between a beam-like component and neighboring constituents of any type with distinct material properties, meaning the complexity of the rest of the multilayered system would not limit the applicability of the *DI*. With the assist of a noncontact laser vibrometry, the proposed approach was validated by detecting multiple debonding zones in a steel-reinforced concrete slab dismantled from a bridge model. Compared with traditional vibration-based detection methods such as those using mode shape curvature, this approach shows higher sensitivity to damage small in dimension because of the use of higher-order derivatives of the vibration signal, which, however, are more vulnerable to noise influence, entailing appropriate proper denoising treatment. The accuracy of the proposed DI can be enhanced in conjunction with the use of denoising treatments such as LWF, AMD, and information fusion. In particular, around 10 measurement points per wavelength can facilitate the achievement of a reasonable balance between the accuracy of finite difference and the noisy immunity of the *DI*.

Declaration of conflicting interests

The authors declare that there is no conflict of interest.

Funding

This project is supported by the Hong Kong Research Grants Council via a General Research Fund (GRF) (No. 523313). This project is also supported by National Natural Science Foundation of China (Grant No. 51375414 and 11272272).

References

1. Wu Z, Qing XP, Ghosh K, et al. Health monitoring of bonded composite repair in bridge rehabilitation. *Smart Mater Struct* 2008; 17(4): 045014 (9 pp.).
2. Taha MM, Choi KK and Azarbayejani M. *Strengthening reinforced concrete bridges in New Mexico using fiber reinforced polymers: report II: design method for strengthening K-frame bridges using FRP*. Report for the New Mexico Department of Transportation, Research Bureau. NM06TT-01, March 2008. Albuquerque, NM: University of New Mexico.
3. Sohn H, Dutta D, Yang JY, et al. Automated detection of delamination and disbond from wavefield images obtained using a scanning laser vibrometer. *Smart Mater Struct* 2011; 20: 045017 (10 pp).
4. Yu T, Fernando D, Teng JG, et al. Experimental study on CFRP-to-steel bonded interfaces. *Compos Part B: Eng* 2012; 43(5): 2279–2289.
5. Ihn J-B and Chang F-K. Detection and monitoring of hidden fatigue crack growth using a built-in piezoelectric sensor/actuator network: II. Validation using riveted joints and repair patches. *Smart Mater Struct* 2004; 13: 621–630.
6. Wu F and Chang F-K. Debond detection using embedded piezoelectric elements for reinforced concrete structures—part I: experiment. *Struct Health Monit* 2006; 5(1): 5–15.
7. Buyukozturk O, Gunes O and Karaca E. Progress on understanding debonding problems in reinforced concrete and steel members strengthened using FRP composites. *Constr Build Mater* 2004; 18(1): 9–19.
8. Ali MSM, Oehlers DJ and Bradford MA. Shear peeling of steel plates adhesively bonded to the sides of reinforced concrete beams. *P I Civil Eng: Str B* 2000; 140(3): 249–259.
9. Soh CK, Tseng KKH and Bhalla S. Performance of smart piezoceramic patches in health monitoring of a RC bridge. *Smart Mater Struct* 2000; 9(4): 533–542.
10. Sohn H, Farrar CR, Hemez FM, et al. *A review of structural health monitoring literature: 1996–2001*. Los Alamos National Laboratory Report. LA-13976-MS, February 2004. Los Alamos, NM: Los Alamos National Laboratory.
11. Rose JL. *Ultrasonic waves in solid media*. New York: Cambridge University Press, 1999.
12. Buyukozturk O and Yu T-Y. Far-field radar NDT technique for detecting GFRP debonding from concrete. *Constr Build Mater* 2009; 23(4): 1678–1689.
13. Worden K, Farrar CR, Manson G, et al. The fundamental axioms of structural health monitoring. *P Roy Soc A: Math Phys* 2007; 463: 1639–1664.
14. Koh CG, Qiao GQ and Quek ST. Damage identification of structural members: numerical and experimental studies. *Struct Health Monit* 2003; 2(1): 41–55.
15. Giurgiutiu V and Cuc A. Embedded non-destructive evaluation for structural health monitoring, damage detection, and failure prevention. *Shock Vib Digest* 2005; 37(2): 83–105.
16. Whittingham B, Li HCH, Herszberg I, et al. Disbond detection in adhesively bonded composite structures using vibration signatures. *Compos Struct* 2006; 75(1–4): 351–363.
17. Shen JY and Sharpe L Jr. An overview of vibration-based nondestructive evaluation techniques. *P SPIE* 1998; 3397: 117–128.
18. Zou Y, Tong L and Steven GP. Vibration-based model-dependent damage (delamination) identification and health monitoring for composite structures—a review. *J Sound Vib* 2000; 230(2): 357–378.
19. Fan W and Qiao P. Vibration-based damage identification methods: a review and comparative study. *Struct Health Monit* 2011; 10: 83–111.
20. Lee YS and Chung MJ. A study on crack detection using eigen-frequency test data. *Comput Struct* 2000; 77: 327–342.
21. Kim JT, Ryu YS, Cho HM, et al. Damage identification in beam-type structures: frequency-based method vs. mode-shape-based method. *Eng Struct* 2003; 25: 57–67.
22. Pandey AK, Biswas M and Samman MM. Damage detection from changes in curvature mode shapes. *J Sound Vib* 1991; 145(2): 321–332.

23. Qiao P, Lu K, Lestari W, et al. Curvature mode shape-based damage detection in composite laminated plates. *Compos Struct* 2007; 80(3): 409–428.
24. Hu N, Wang X, Fukunaga H, et al. Damage assessment of structures using modal test data. *Int J Solids Struct* 2001; 38: 3111–3126.
25. Hu N, Fukunaga H, Kameyama M, et al. Vibration analysis of delaminated composite beams and plates using a higher-order finite element. *Int J Mech Sci* 2002; 44(7): 1479–1503.
26. Ayres JW, Lalande F and Chaudhry Z. Qualitative impedance-based health monitoring of civil infrastructures. *Smart Mater Struct* 1999; 7(5): 599–605.
27. Giurgiutiu V and Rogers CA. Recent advancements in the electro-mechanical (E/M) impedance method for structural health monitoring and NDE. *P SPIE: Smart Struct Mater* 1998; 3329: 536–547.
28. Pandey AK and Biswas M. Damage detection in structures using changes in flexibility. *J Sound Vib* 1994; 169(1): 3–17.
29. Aoki Y, Byon OI and Ben G. Damage detection of CFRP pipes and shells by using localized flexibility method. *Adv Compos Mater* 2001; 10: 189–198.
30. Yan A and Golinval JC. Structural damage localization by combining flexibility and stiffness methods. *Eng Struct* 2005; 27: 1752–1761.
31. Kawiecki G. Modal damping measurement for damage detection. *Smart Mater Struct* 2001; 10: 466–471.
32. Farrar CR, Doebling SW and Nix DA. Vibration-based structural damage identification. *Philos T Roy Soc A* 2001; 359: 131–149.
33. Pezerat C and Guyader JL. Two inverse methods for localization of external sources exciting a beam. *Acta Acust* 1995; 3: 1–10.
34. Pezerat C and Guyader JL. Force analysis technique: reconstruction of force distribution on plates. *Acta Acust United Ac* 2000; 86: 322–332.
35. Xu H, Cheng L, Su Z, et al. Identification of damage in structural components based on locally perturbed dynamic equilibrium. *J Sound Vib* 2011; 330(24): 5963–5981.
36. Xu H, Cheng L, Su Z, et al. Damage visualization based on local dynamic perturbation: theory and application to characterization of multi-damage in a plane structure. *J Sound Vib* 2013; 332(14): 3438–3462.
37. Su Z, Wang X, Cheng L, et al. On selection of data fusion schemes for structural damage evaluation. *Struct Health Monit* 2009; 8: 223–241.
38. Zhou C, Su Z and Cheng L. Probability-based diagnostic imaging using hybrid features extracted from ultrasonic lamb wave signals. *Smart Mater Struct* 2011; 20: 125005 (14 pp.).